J. Fluid Mech. (2006), *vol.* 555, *pp.* 459–473.
doi:10.1017/S0022112006008950 Printed in the United Kingdom

The evolution of a finite-amplitude localized disturbance in an irrotational unbounded plane stagnation flow

By JIMMY PHILIP AND JACOB COHEN

Faculty of Aerospace Engineering, Technion – I.I.T., Haifa, 32000, Israel

(Received 17 August 2005 and in revised form 19 December 2005)

The evolution of a finite-amplitude three-dimensional localized disturbance, having an initial dipole Gaussian vorticity distribution, embedded in an external unbounded irrotational plane stagnation flow ($\boldsymbol{U} = (Ay, Ax, 0)$) is investigated. Using the fluid impulse integral as a characteristic of such a disturbance, the viscous vorticity equation is integrated analytically. Accordingly, the fluid impulse associated with such disturbances decays and grows exponentially along the principal axes $x = y$ and $x = -y$, respectively. Numerical simulations, carried out for both linear and nonlinear disturbances at a Reynolds number of 40, confirm the above predictions. The simulations have also been compared with the solution of the linear viscous vorticity disturbance equation. While the solution predicts the vorticity distribution for the linear case, it fails to predict the essential characteristics of a nonlinear disturbance associated with its self-induced movement. Finally, it is shown that the fluid impulse and the disturbance kinetic energy follow the same trend, i.e. when the fluid impulse increases with time so does the kinetic energy and vice versa. The correspondence between them suggests the use of the fluid impulse to predict the stability of a localized disturbance.

1. Introduction

The evolution of a finite-amplitude three-dimensional localized disturbance, having an initial dipole Gaussian vorticity distribution, embedded in an external irrotational unbounded plane stagnation flow is the subject of the present study. On one hand, this problem is practically useful in the study of drop deformation and breakup (e.g. the famous 'four roll mill' experiment by Taylor 1934). On the other hand, the simplicity of the base flow, the strain matrix of which is constant, makes it easily amenable to many theoretical studies such as stability analysis (Wilson & Gladwell 1978; Lagnado, Phan-Thien & Leal 1984; Lyell & Huerre 1985; Farrell 1989; Brattkus & Davis 1991; Kerr & Dold 1994; Criminale, Jackson & Lasseigne 1994), turbulent flows using rapid distortion theory where it is assumed that the turbulence has no effect on the straining flow (e.g. Kevlahan & Hunt 1997), modelling of turbulent mixing layers (Lin & corcos 1984), and the possibility of getting exact solutions of Navier–Stokes (Craik & Criminale 1986) and Euler (Kida 1981; Neu 1984) equations.

In the following, the stability of plane stagnation flows is briefly reviewed. The review is categorized according to the initial disturbance type, either *wavelike* or *localized* in space, and according to the confinement of the base stagnation flow, either *bounded*, in which the stagnation points are located at boundaries, or *unbounded*, in which free stagnation lines are located in the bulk of the fluid.

Traditionally the disturbance is assumed to be wavelike. Wilson & Gladwell (1978) theoretically investigated the stability of two-dimensional viscous bounded stagnation-point flow with respect to three-dimensional infinitesimal disturbances which are periodic in the direction perpendicular to the plane of the flow. They found that these disturbances, in the limit of infinite Reynolds number, are stable. Lyell & Huerre (1985) considered the same situation but with finite-amplitude disturbances. Accordingly, two- and three-mode interaction models, based on the least-damped modes of the linear theory, indicate that three-dimensional fluctuations can be triggered to grow exponentially above a certain threshold. Brattkus & Davis (1991) considered the linear stability of a wider class of disturbances and found no solution with growth rates that are larger than those of Wilson & Gladwell (1978).

The linear stability of two-dimensional unbounded stagnation flow was studied by Lagnado *et al.* (1984) as a special case of a wider class of two-dimensional linear flows. They found that an arbitrary spatially periodic wavelike initial viscous disturbance, at large times grows exponentially and oriented along the principal axis of the extensional strain. Kerr & Dold (1994) applied nonlinear numerical analysis to a similar situation and showed that the vorticity components of three-dimensional disturbances that are initially perpendicular to the diverging flow will decay, and that the parallel component of vorticity can grow. Andreotti, Douady & Couder (2001) have demonstrated experimentally that pure straining flow becomes intrinsically unstable. Moreover, near the critical Reynolds number the transverse velocity profiles of the vortical disturbances are in agreement with those predicted numerically by Kerr & Dold (1994).

Farrell (1989) considered the linear evolution of two-dimensional disturbances in two-dimensional unbounded flows. He considered both kinds of disturbances: an initial plane wave and a disturbance having initially a symmetrical Gaussian distribution of vorticity. He found that the energy of a single plane wave can grow whereas the other two-dimensional localized disturbance is stable. It was also found that spatially asymmetric disturbances can experience an initial transient growth of energy before approaching a constant value. Criminale *et al.* (1994) studied the linear evolution of three-dimensional disturbances in a three-dimensional bounded stagnation flow. In particular, when considering the energy of a localized disturbance having an even-function Gaussian distribution of its initial vorticity, it was found that the planar stagnation-point flow represents a neutrally stable flow whereas the three-dimensional flow is either stable or unstable.

The main objective of the present paper is to study, using the fluid impulse (FI) integral, the stability of viscous irrotational unbounded plane stagnation flow with respect to a finite-amplitude three-dimensional localized disturbance, having an initial dipole Gaussian vorticity distribution. Moreover, it is intended to show that the fluid impulse is a suitable characteristic to describe the growth (or decay) of such localized disturbances. The fluid impulse, $\boldsymbol{p}$, is defined as:

$$\boldsymbol{p} = \frac{1}{2}\int \boldsymbol{x} \times \boldsymbol{\omega}(\boldsymbol{x})\,\mathrm{d}V, \tag{1.1}$$

where the bold type indicates vector character, $\boldsymbol{x}$ is the position vector, $\boldsymbol{\omega}$ is the vorticity vector, $\mathrm{d}V$ is a volume element and the integral is taken over the whole fluid. In unbounded three-dimensional flows, the FI is not modified by self-induced motion (Batchelor 1967) or by viscous effects. Consequently, the evolution of the FI satisfies a linear equation, even though the fluid motion itself is governed by nonlinear effects. Although the integral character of the FI does not provide the details of the flow within the disturbance vortical region, this insensitivity yields, in turn, some universal properties.

The rest of the paper is organized as follows. Theoretical aspects concerning the evolution of the fluid impulse are described in § 2. The numerical procedure and the computational details are presented in § 3. Section 4 contains a comparison of a linear analytical solution (Leonard 2000) and the numerical simulations. Also presented are the results for the evolution of the fluid impulse integral obtained numerically and compared with the corresponding theoretical prediction for linear and nonlinear cases. The main results are presented and discussed in § 5 and the main conclusions are given in § 6.

2. Some theoretical considerations

Here we follow previous studies in which the fluid impulse was used to describe the evolution of vortical structures. Roberts (1972) applied the FI to an inviscid flow consisting of a set of small interacting circular vortex rings separated by a large distance relative to their dimensions, whereas Levinski & Cohen (1995) used it to follow the evolution of a localized disturbance in inviscid shear flows. In the following we apply a similar model to the particular case in which a finite-amplitude viscous three-dimensional localized disturbance is embedded in an unbounded two-dimensional irrotational stagnation-point flow for which the velocity field is $\boldsymbol{U}=(Ay, Ax, 0)$, where (x, y, z) are the coordinates in the Cartesian system and A is a positive constant.† The resultant disturbance vorticity equation is

$$\frac{\partial \boldsymbol{\omega}}{\partial t}+(\boldsymbol{U}\cdot\nabla)\boldsymbol{\omega}-(\boldsymbol{\omega}\cdot\nabla)\boldsymbol{U}+(\boldsymbol{u}\cdot\nabla)\boldsymbol{\omega}-(\boldsymbol{\omega}\cdot\nabla)\boldsymbol{u}-\nu\Delta\boldsymbol{\omega}=0, \tag{2.1}$$

where the disturbance vorticity $\boldsymbol{\omega}$ and velocity $\boldsymbol{u}$ are related by $\boldsymbol{\omega}=\nabla\times\boldsymbol{u}$. It is assumed that $\boldsymbol{\omega}(t=0)$ is localized in space. In order to study the development of the initial localized vorticity disturbance, we follow the evolution of its FI. Using (2.1) and (1.1), we obtain

$$\frac{\mathrm{d}\boldsymbol{p}}{\mathrm{d}t}=-\frac{1}{2}\lim_{R_1\to\infty}\int_{|\boldsymbol{x}|\leqslant R_1}\boldsymbol{x}\times[(\boldsymbol{U}\cdot\nabla)\boldsymbol{\omega}-(\boldsymbol{\omega}\cdot\nabla)\boldsymbol{U}+(\boldsymbol{u}\cdot\nabla)\boldsymbol{\omega}-(\boldsymbol{\omega}\cdot\nabla)\boldsymbol{u}-\nu\Delta\boldsymbol{\omega}]\,\mathrm{d}V, \tag{2.2}$$

where, for convenience, a spherical volume with a radius $R_1\to\infty$ is used.

The first four integrals on the right-hand side of (2.2) are similar to those evaluated in Appendix A of Levinski & Cohen (1995). By transformation to surface integrals the nonlinear terms as well as the viscous term

$$\begin{aligned}\int_{|\boldsymbol{x}|\leqslant R_1}\varepsilon_{ijk}x_j\frac{\partial^2\omega_k}{\partial x_l\partial x_l}\,\mathrm{d}V&=\varepsilon_{ijk}\int_{|\boldsymbol{x}|\leqslant R_1}\left\{\frac{\partial^2(\omega_k x_j)}{\partial x_l\partial x_l}-2\frac{\partial\omega_k}{\partial x_j}\right\}\mathrm{d}V\\&=\varepsilon_{ijk}\left\{\oint_{|\boldsymbol{x}|=R_1}\frac{\partial(\omega_k x_j)}{\partial x_l}n_l\,\mathrm{d}S-2\oint_{|\boldsymbol{x}|=R_1}\omega_k n_j\,\mathrm{d}S\right\}.\end{aligned}$$

vanish in the evolution of the FI. So the only contribution to the evolution of the FI is from the first two integrals. Consequently, for $\boldsymbol{U}=(Ay, Ax, 0)$ equation (2.2) becomes‡

$$\frac{\mathrm{d}p_x}{\mathrm{d}t}=-p_yA,\quad \frac{\mathrm{d}p_y}{\mathrm{d}t}=-p_xA,\quad \frac{\mathrm{d}p_z}{\mathrm{d}t}=0. \tag{2.3}$$

† It should be noted the conventional definition of an irrotational stagnation-point flow which is given by $\boldsymbol{U}=(Ax, -Ay, 0)$ is merely a pure rotation of our coordinate system by 45°. The reason for this is to extend the principal axes in the computational domain.

‡ This equation can also be derived from equation 12 on p. 50 of Saffman (1992) by excluding body forces and dividing the velocity and vorticity fields into base and disturbance fields.

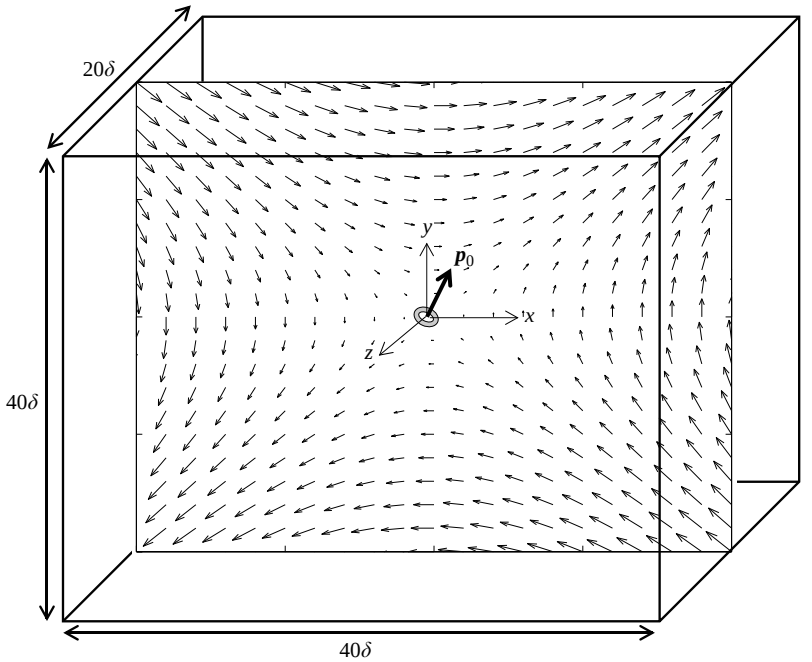

FIGURE 1. A schematic of the computational domain including the base flow and the initial Gaussian disturbance.

If x_1 and x_2 are the principle axes along $x = y$ and $x = -y$, respectively, the evolution of the corresponding components of the fluid impulse (p_{x_1} and p_{x_2}) is

$$p_{x_1} = p_{x_{10}} \mathrm{e}^{-At}, \quad p_{x_2} = p_{x_{20}} \mathrm{e}^{At}, \quad p_z = 0, \tag{2.4}$$

where subscript 0 denotes value at time $t = 0$ and $p_{z0} = 0$. It is noted here that in terms of the regular coordinates, the vectors, $\boldsymbol{p}_{x_1} = \boldsymbol{p}_y + \boldsymbol{p}_x$ and $\boldsymbol{p}_{x_2} = \boldsymbol{p}_y - \boldsymbol{p}_x$.

3. Numerical procedure

The equations of motion are solved numerically using the finite volume solver FLUENT. First, the steady base flow ($\boldsymbol{U} = (Ay, Ax, 0)$) is obtained and then a localized disturbance is superimposed onto the base flow at time $t = 0$, the evolution of which is then monitored. The initial localized disturbance has a dipole vorticity distribution and is similar to that used by Suponitsky, Cohen & Bar-Yoseph (2005):

$$\boldsymbol{\omega} = -\boldsymbol{p} \times \nabla F, \qquad F = \left(\pi^{1/2}\delta\right)^{-3} \exp\left(-r_s{}^2/\delta^2\right), \tag{3.1}$$

where $\boldsymbol{\omega}$ is the vorticity vector and $\boldsymbol{p}$ defines its space orientation given by (1.1). F in (3.1) is normalized such that $\int_V F \, \mathrm{d}V = 1$, r_s is a spherical radial coordinate and δ is a representative length scale of the disturbance. All lengths are normalized by δ, i.e. $X = x/\delta$, $Y = y/\delta$ and $Z = z/\delta$, and time by A as $T = tA$. The magnitude of the disturbance is defined as $\varepsilon = \omega_{max}/A$, where ω_{max} is the maximum magnitude of vorticity of the initial disturbance.

The computational domain along with the base velocity profile at $z = 0$ and the initial Gaussian disturbance ($\boldsymbol{p} = \boldsymbol{p}_0$) placed at the origin are schematically shown in figure 1. The extent of the computational domain is $40\delta \times 40\delta \times 20\delta$ in the x-, y- and z-directions, respectively. The simulation is done with half a million grid points.

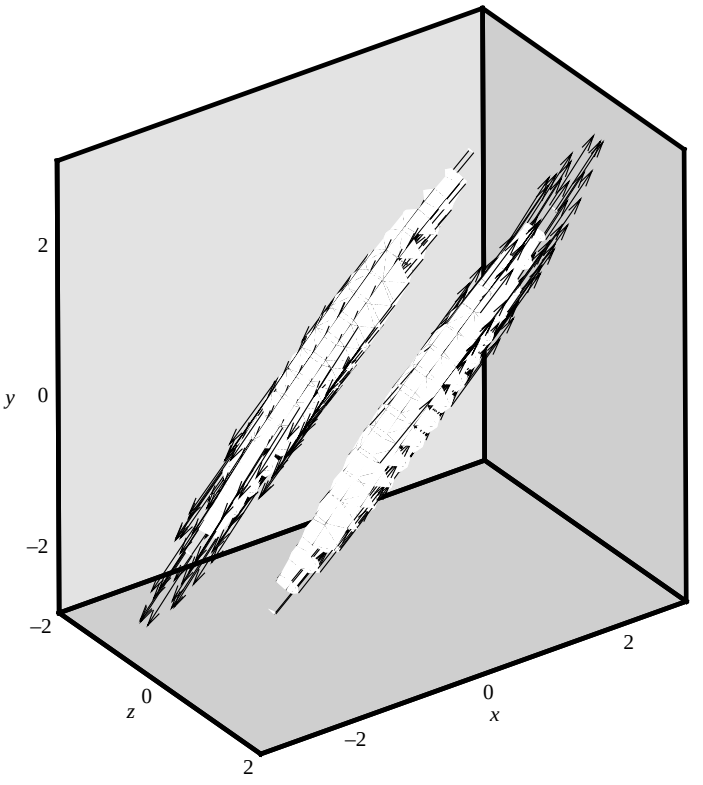

FIGURE 2. Iso-surfaces of the vorticity magnitude ($\| \boldsymbol{\omega} \| / \omega_{max} = 0.7$) and the associated vorticity vectors at time $T = 2.0$ for $\varepsilon = 0.015$.

A further increase in the number of grid points and/or a further extension of the computational domain had no significant effect on the results. The distribution of the grid points is denser in the region surrounding the disturbance, having about 5–6 volume elements per disturbance length scale δ in all directions. The distance separating the neighbouring grid points increases towards the boundary of the domain. The base flow is obtained by using appropriate boundary conditions of velocity inlet and gauge pressure outlet in the X- and Y-directions. Owing to the symmetry of the equations and the initial disturbance, the flow field is symmetric about the z-axis.

4. Results

4.1. *The evolution of a small-amplitude disturbance* ($\varepsilon \ll 1$)

4.1.1. *Comparison between Leonard's analytical solution and the numerical results*

A typical structure for a linear disturbance ($\varepsilon = 0.015$) initially placed horizontally ($p_x = 0$, $p_y = p_{y0}$ and $p_z = 0$) is shown in figure 2 at $T = 2.0$. The structure seen is that of a counter-rotating vortex pair (CVP), which is stretched along the direction of the principal axis $x = y$.

A comparison between the analytical, viscous and inviscid solutions of the three-dimensional linearized vorticity equation obtained by Leonard (2000) for an initial Gaussian vortex in an irrotational flow, and the numerical solution of the full Navier–stokes equations for a relatively small amplitude ($\varepsilon = 0.015$) is shown in figure 3. The

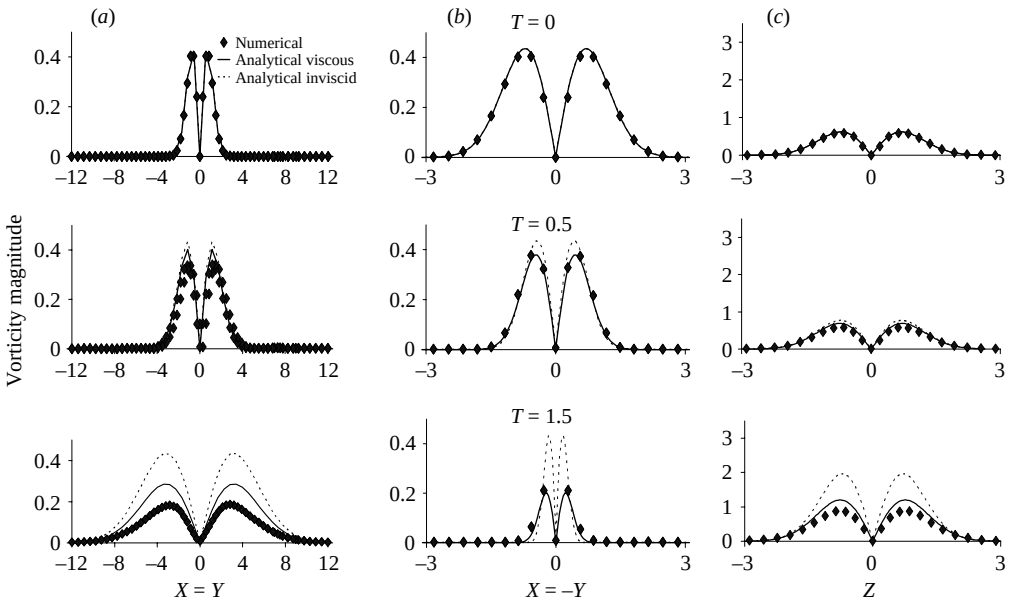

FIGURE 3. Comparison between the linear theory (Leonard 2000) and numerical results ($\varepsilon = 0.015$). Temporal evolution of vorticity magnitude of an initially Gaussian disturbance, (a) along $X = Y$, (b) along $X = -Y$ and (c) along Z-axis.

analytical solution of Leonard (2000) for the vorticity field is

$$\boldsymbol{\omega}(\boldsymbol{x}, t) = \nabla \times \left\{ \boldsymbol{a}(t)\delta^3 (\det \boldsymbol{M})^{1/2} \exp[-(\boldsymbol{F}^{-1}\boldsymbol{M}\boldsymbol{F}^{\boldsymbol{T}-\boldsymbol{1}}) \ : (\boldsymbol{x})(\boldsymbol{x})] \right\}, \tag{4.1}$$

where $\boldsymbol{F}$ is the deformation tensor, $\boldsymbol{M}$ is the tensor that includes viscous effects and $\boldsymbol{a}$ is the vector related to the fluid impulse. The distributions of the vorticity magnitude along the principal axes $X = Y$, $X = -Y$ and along the Z-axis are shown in figure 3 (a, b, c), respectively. The viscous analytical solution for $Re \equiv A\delta^2/\nu = 40$, where ν is the kinematic viscosity of the fluid, is shown by the solid lines, the inviscid analytical solution by the dashed lines and the corresponding numerical viscous solution is shown by symbols.

It is evident that the viscous numerical solution follows closely the analytical solution along the $(X = -Y)$-axis during the entire evolution (up to $T = 2$). The numerical solutions for the magnitude of vorticity along the $(X = Y)$- and Z-axes also follow the analytical ones although they are somewhat smaller. With time the difference between the two increases. Based on the results of additional simulations we attribute these deviations to the presence of a small nonlinearity. Very low-amplitude disturbances could not be studied because of numerical errors, associated with obtaining a pure irrotational base flow. While the shape of the vorticity magnitude distribution is preserved well by the inviscid solutions, its magnitude is severely overestimated. Finally it is observed that the vorticity magnitude along the principal axes reduces with time while that along the Z-axis increases.

4.1.2. *The evolution of the fluid impulse*

To verify the theoretical prediction (2.4), the fluid impulse is calculated from numerical data and compared with the theoretical solution. In the present case the far-field vorticity always vanishes and therefore the fluid impulse integral is

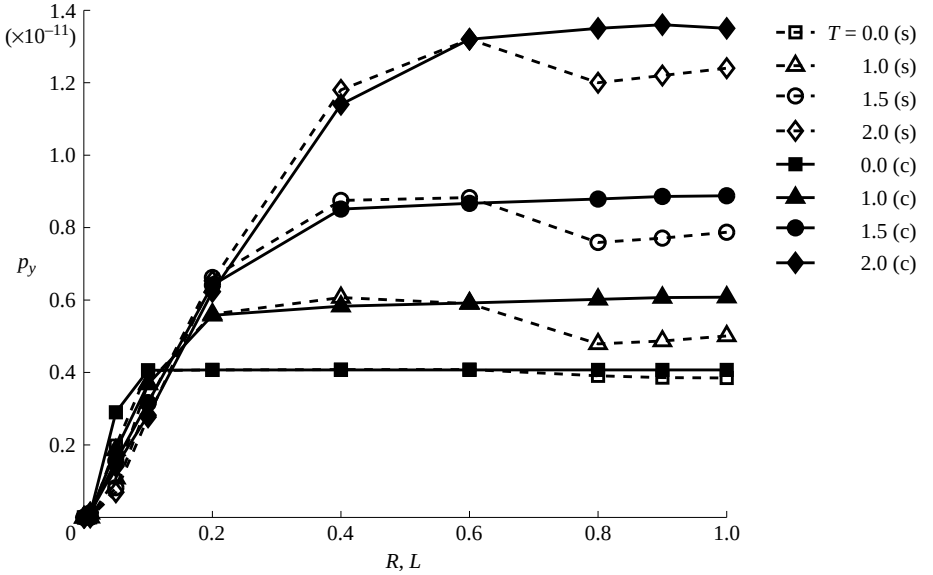

FIGURE 4. p_y integrated within a spherical volume (s) of radius R and a cylindrical volume (c) with axis length L as a function of R and L, respectively, where $[p_{x_0} = 0,\ p_{y_0} = 4 \times 10^{-12},\ p_{z_0} = 0]$.

absolutely convergent. We first calculate it with the volume of integration increasing spherically from its centre at the origin. Since the numerically obtained base flow is not completely irrotational (as some small vorticity caused by the finite geometry and the boundary conditions is still present at the edges of the computational domain), the integral is also calculated within a cylindrical region. The generators of the cylinder are parallel to the line $X = Y$ with centre at the origin. This avoids the edges of the computational domain during the integration whereas the disturbance and its surrounding are included. The value of the integral p_y as a function of R and L is shown in figure 4 (with $\varepsilon = 0.015$ and $Re = 40$), where R and L are the normalized (by their maximum dimensional values) sphere radius and cylinder height. It can be seen that the integral converges smoothly for the cylindrical domain but not for the spherical one. Therefore, the cylindrical domain is used for all further evaluation of the fluid impulse.

The solution for p_{x_1} and p_{x_2}, normalized by $|\boldsymbol{p}_0|$, are obtained from (2.4) subject to the initial conditions specified above ($p_x = 0,\ p_y = p_{y_0}$ and $p_z = 0$). It is compared with the results of the numerical simulation in figure 5. The numerical solution for the linear case ($\varepsilon = 0.015$) is shown with symbols (p_{x_1} with an open square and p_{x_2} with a solid square) and the analytical prediction by lines (p_{x_1} with dashed and p_{x_2} with solid). The comparison is made only till $T = 2$ because beyond this time the edges of the vortical structure are extended outside the computational domain. The numerical results follow closely the theoretical predictions. Both p_{x_1} and p_{x_2} decrease and increase exponentially with the same exponents A.

For times much greater than $(1/A)$ and for a given orientation of the initial vortex in the (X, Y)-plane, the exponentially growing components (p_{x_2}) become dominant and, consequently, the long-time orientation of the vortical structure is along the principal axis $X = Y$. The confirmation of this prediction can be deduced from the long-time orientation of the vortex pair in figure 2. Finally, it should be noted that

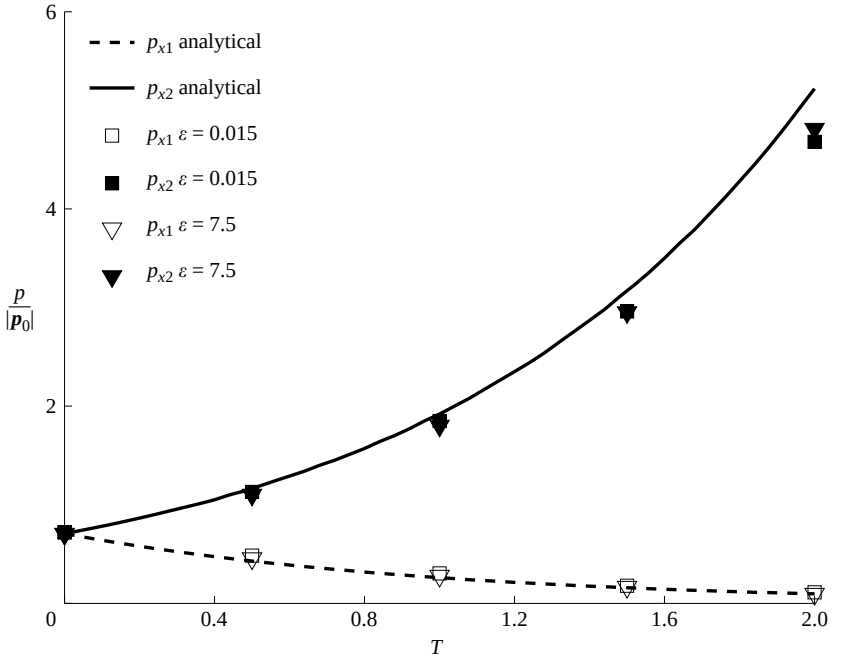

FIGURE 5. Comparison between the prediction of (2.4) and the numerical results (symbols) for linear ($\varepsilon = 0.015$) and nonlinear ($\varepsilon = 7.5$) evolution of the normalized fluid impulse.

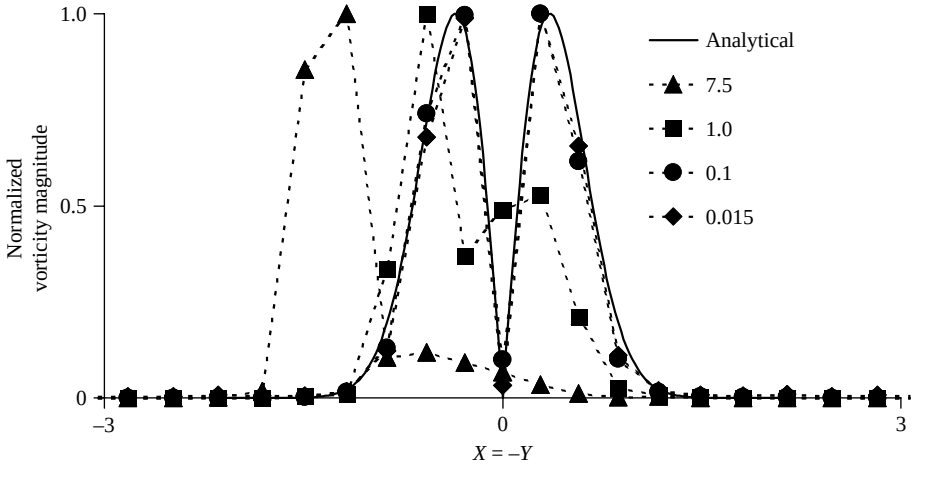

FIGURE 6. Comparison between the linear theory (Leonard 2000) and numerical results for $\varepsilon = 0.015, 0.1, 1.0, 7.5$ at $T = 1$. Vorticity magnitude distribution along $X = -Y$ (X_2).

according to (2.4), p_z should not change. This is indeed the situation for the particular case solved numerically and discussed above for which p_z remains zero.

4.2. *The evolution of a large-amplitude disturbance* ($\varepsilon = 7.5$)

The results of the numerical simulation for the nonlinear case ($\varepsilon = 7.5$) are compared with the linear analytical solution of Leonard (2000). Figure 6 shows the normalized

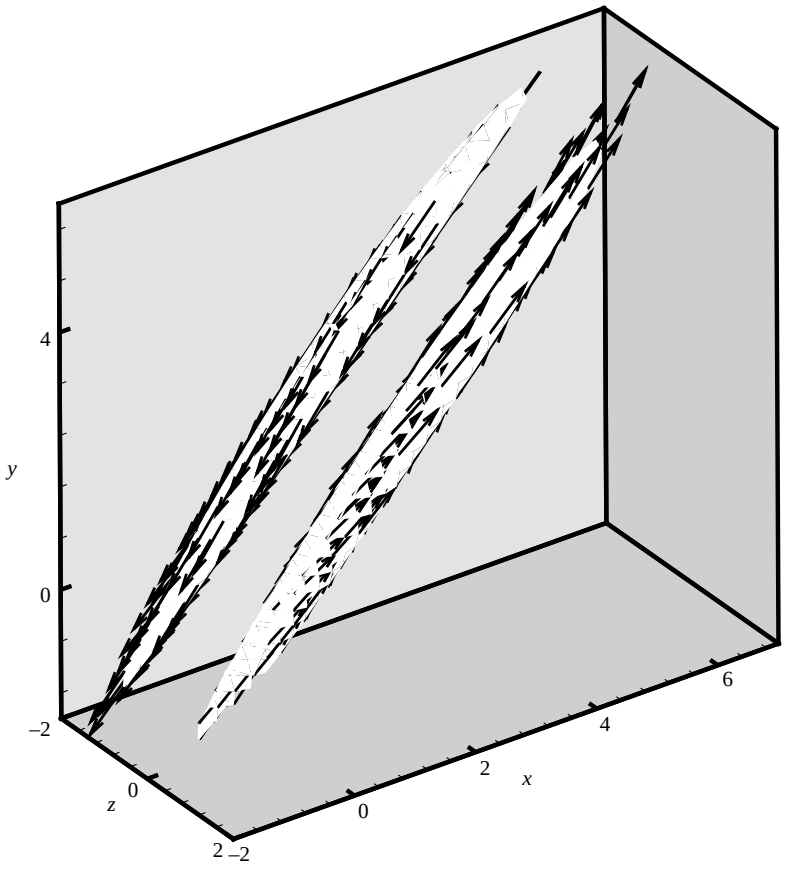

FIGURE 7. Iso-surfaces of the vorticity magnitude ($\| \boldsymbol{\omega} \| / \omega_{max} = 0.7$) and the associated vorticity vectors at time $T = 2.0$ for $\varepsilon = 7.5$.

vorticity magnitude ($\omega/(\omega_{max}(T=1))$ plotted along $X = -Y$ (X_2) for various values of ε, ranging from the linear case of $\varepsilon = 0.015$ to $\varepsilon = 7.5$ at time $T = 1$. The typical character of the nonlinear nature of the disturbance is seen during the symmetry breaking which happens as the value of ε is increased beyond 0.1. Even at $\varepsilon = 0.1$ (at $X_2 = 0$) the nonlinear behaviour associated with the self-induced velocity of the disturbance can be noticed, where there is a slight 'lift-up' of the disturbance. The lift-up effect is most noticeable along X_2, as this is the main direction of the self-induced velocity. With the increase in ε, this lift-up has a pronounced effect, eventually causing the vortex structure to move along X_2, breaking the symmetry of its associated vorticity distribution. A three-dimensional view of the structure is shown in figure 7. The structure is very similar to the 'linear' one, having a pair of counter-rotating vortices stretched along the X_1-direction. The shift of the disturbance from its origin (due to its self-induced motion) and the presence of asymmetry in the numerical solution (figure 6) are clear indications of nonlinear effects.

The predictions of the temporal evolution of the fluid impulse are compared with numerical simulations for initial conditions identical to the ones used for the linear case except that initial amplitude is $\varepsilon = 7.5$. The comparison is shown in figure 5. As in the linear case, the numerical results for the nonlinear case follow closely the theoretical prediction.

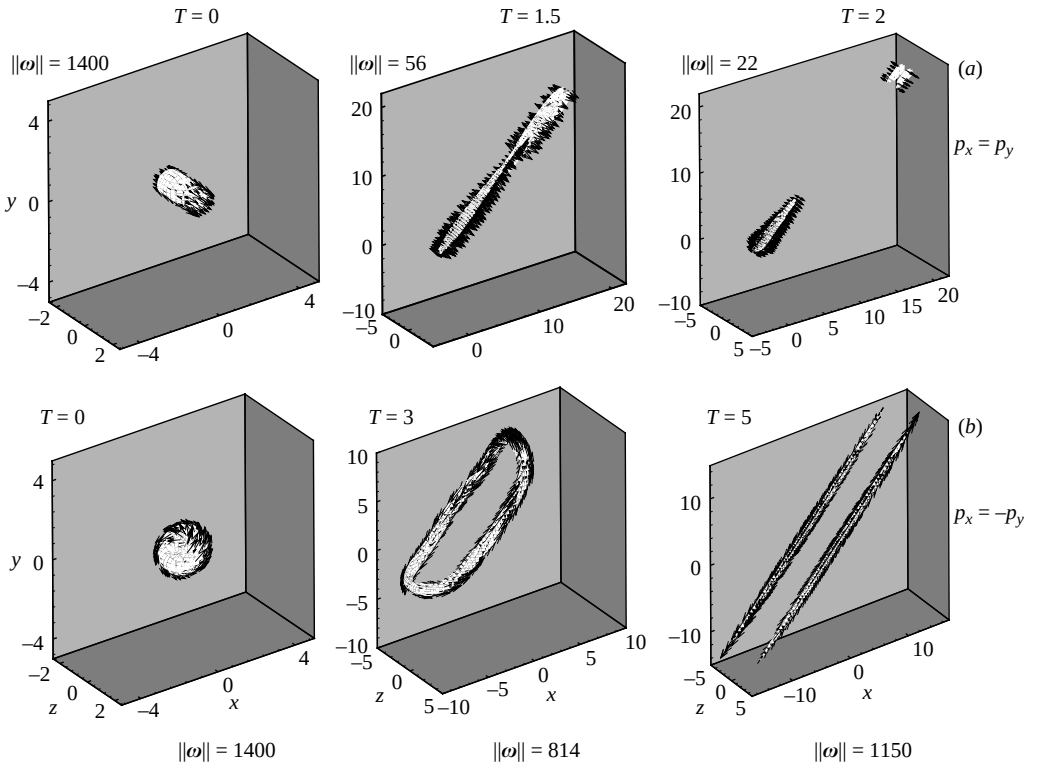

FIGURE 8. Iso-surfaces of the vorticity magnitude ($\| \boldsymbol{\omega} \| / \omega_{max} = 0.7$) and the associated vorticity vectors for $\varepsilon = 50$. (a) Case (a) $p_0 = p_{x_{10}}$, (b) case (b) $p_0 = p_{x_{20}}$.

4.3. *Evolution of highly nonlinear* ($\varepsilon = 50$) *Gaussian disturbances initially along the principal axes*

In this section we examine the predictions of (2.4) for two cases in which the initial vortex is highly nonlinear ($\varepsilon = 50$) and its initial FI is along the principal axis X_1 (case a), and along X_2 (case b). The temporal evolution of cases (a) and (b) is presented in figures 8(a) and 8(b), respectively, by the iso-surfaces of the vorticity magnitude (the values of which are shown for each time instance). Also presented are the associated vorticity vectors, indicated by the black arrows. The evolution of the fluid impulse corresponding to cases (a) and (b) is shown in figure 9(a) and 9(b), respectively. The theoretical predictions (lines) agree well with the numerical results (symbols). Accordingly, the fluid impulse decays and grows exponentially along X_1 and X_2, respectively.

In figure 8(a) the induced velocity (which initially is very high) is in the same direction as the base flow (along X_1). Consequently the structure moves rapidly away from its origin. This motion is depicted in figure 10, which shows the movement of the centre of the vortex structure (CVS) along X_1 by filled symbols. The CVS ($X_{cvs_i}(t)$) is defined as the first moment of enstrophy divided by the total enstrophy: $X_{cvs_i}(t) = [\int_V \|\boldsymbol{\omega}(t)\|^2 x_i \mathrm{d}V]/W(t)$, where $W(t)$ is the enstrophy given by $W(t) = \int_V \|\boldsymbol{\omega}(t)\|^2 \mathrm{d}V$. The structure is stretched rapidly (until it is split into two) whereas the direction of its associated vorticity remains along its circumference. Consequently, the area normal to the vorticity vectors increases and therefore the vorticity magnitude decreases. As the vorticity in the cross-section normal to X_1 decreases rapidly while

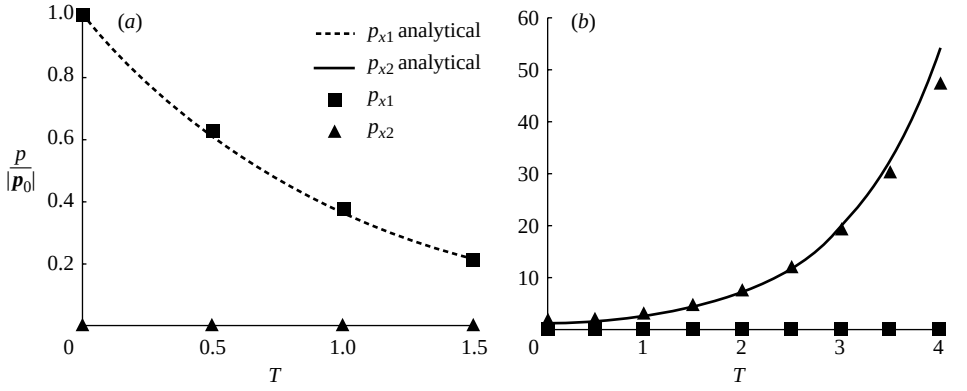

FIGURE 9. Comparison of fluid impulse prediction from numerical simulation and analytical solution (2.4). (*a*) $p_0 = p_{x_{10}}$, (*b*) $p_0 = p_{x_{20}}$.

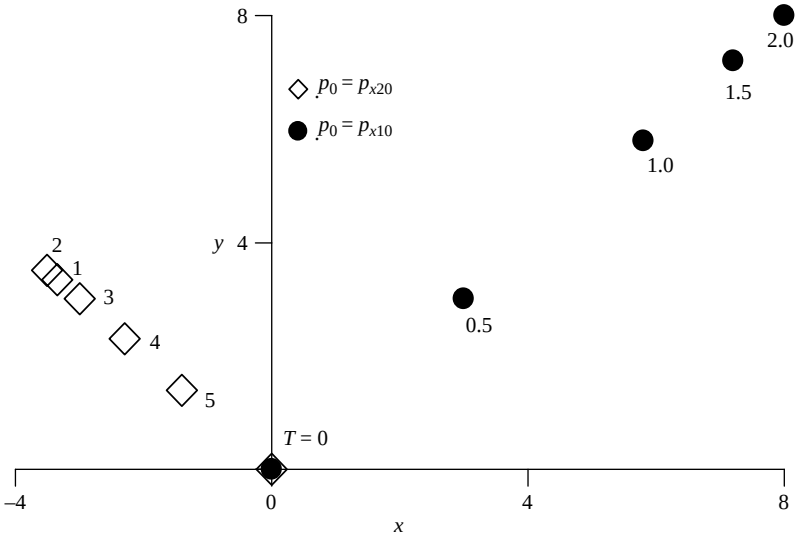

FIGURE 10. The movement of the centre of the vortical structure ($X_{cvs_1}(t)$ along the x-axis and $X_{cvs_2}(t)$ along the y-axis) with time for $\varepsilon = 50$. ●, case (*a*) $p_0 = p_{x_{10}}$ and ◇, case (*b*) $p_0 = p_{x_{20}}$.

the size of the cross-section decreases only a little, $p_{x_1} = \frac{1}{2}\int(x_2\omega_3 - x_3\omega_2)\mathrm{d}V$ should decrease. The decrease in vorticity is accompanied by an almost exponential decrease in the enstrophy (figure 12 below).

In figure 8(*b*), the initial induced velocity is in the direction of X_2, opposite to the base flow ($-X_2$). Owing to its high initial induced velocity the structure at initial times moves rapidly along X_2 (shown in figure 10 by open symbols). As it moves upward, the size of the dipole vortex as well as its core increases rapidly. The increase of the vortex size is evident from figure 11 where the temporal growth of the spanwise distance between the two vorticity maxima (D) is plotted. Consequently, the induced velocity is reduced drastically, and by $T \approx 2$ it equals to that of the opposing base flow. This results in the stopping of the structure and its slow movement back towards its original position (see figure 10) as its dimensions continue to increase. Despite its

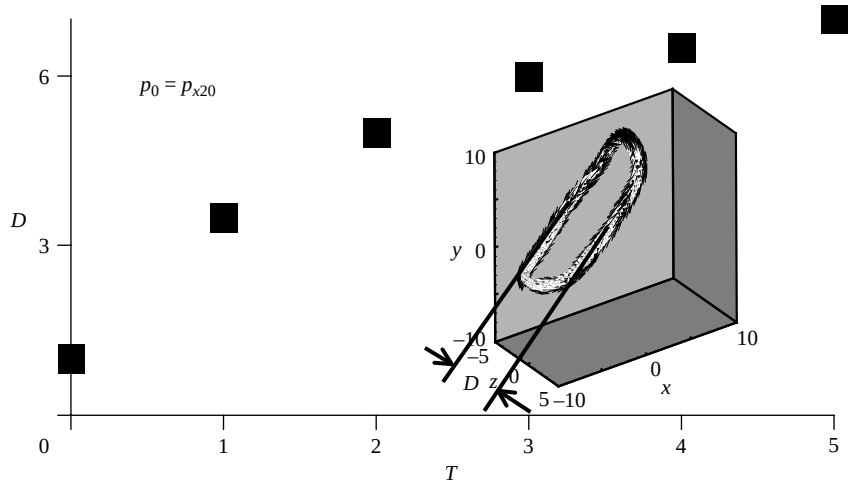

FIGURE 11. Normalized spanwise distance between the two vorticity maxima of the vortex structure for $\varepsilon = 50$, in case (b) $p_0 = p_{x_{20}}$.

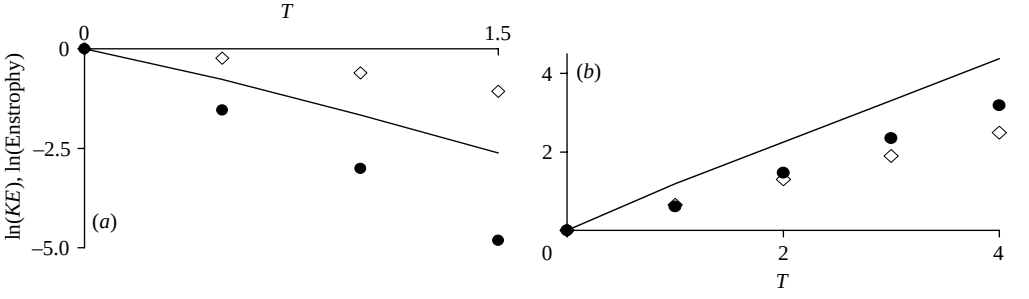

FIGURE 12. Evolution of the KE (●) and enstrophy (◇) for (a) $p_0 = p_{x_{10}}$ and (b) $p_0 = p_{x_{20}}$. Numerical simulations for $\varepsilon = 50$ (symbols) and KE using inviscid linear theory (solid lines).

stretching during the upward movement, the vorticity decreases a little due to the increase in core size. As the vortex moves backward it transforms into a CVP and its movement is slowed down. This is due to the fact that the distance D increases slowly and the induced velocity decreases as $\approx 1/D$. During this time ω_1 continues to increase due to vortex stretching. Thus, the evolved structure is that of a CVP aligned with X_1. It is interesting to note that when the spacing between its legs, D, is expressed in terms of wall units, it is about 45 (at $T = 5$) which is close to the distance observed between the legs of CVPs commonly occurring in turbulent boundary layers. During the whole duration the enstrophy continues to increase at a near exponential rate as seen in figure 12(b). The growth of FI during the upward movement is mainly due to the growth of the vortex dimensions whereas at subsequent times it is due to vortex stretching.

5. Discussion

In this paper we have examined the evolution of a finite-amplitude three-dimensional localized disturbance, having an initial dipole Gaussian vorticity distribution, embedded in an external irrotational unbounded plane stagnation flow. It has

been shown that independent of its initial amplitude, the vortex structure is stretched along X_1 and compressed along X_2. This is in agreement with the previous study of Marshal & Grant (1994) where they showed numerically that a vortex ring subjected to an external straining flow elongates in the direction of stretching of this flow. Similar results obtained from a viscous linear stability analysis were also reported by Lagnado *et al.* (1984) in which the vorticity component ω_1 along the principle axis of extensional strain increases at an exponential rate due to vortex line stretching. Kida (1981) for a two-dimensional elliptic vortex in two-dimensional stagnation flow and Neu (1984), as a special case of three-dimensional stagnation flow, solved the Euler equation exactly and found that when the strain is very strong, the vortex is always elongated infinitely in the direction of strain. This general behaviour is similar to what we have observed in our case with a three-dimensional vortex in a two-dimensional stagnation flow.

For the two-dimensional stagnation flow considered in the present study, the base flow, when transformed along the principal axes, becomes $\boldsymbol{U} = (Ax_1, -Ax_2, 0)$. The evolution of an inviscid small-amplitude vortical disturbance is then given by $\mathrm{D}\omega_1/\mathrm{D}t = \omega_1 A$, and $\mathrm{D}\omega_2/\mathrm{D}t = -\omega_2 A$, and $\mathrm{D}\omega_3/\mathrm{D}t = 0$ where $\mathrm{D}/\mathrm{D}t$ is the material derivative. Thus, the basic mechanism is that ω_1 increases exponentially along X_1 due to stretching while ω_2 decays at the same rate along X_2 due to compression. This mechanism can be used to give a qualitative picture of the evolution of the fluid impulse in the X_1 $(p_{x_1} = \frac{1}{2}\int(x_2\omega_3 - x_3\omega_2)\mathrm{d}V)$ and X_2 $(p_{x_2} = \frac{1}{2}\int(x_3\omega_1 - x_1\omega_3)\,\mathrm{d}V)$ directions for the 'linear case'. Apart from the exponential evolution of the vorticity of a material element, a similar growth rate in the position of such an element (e^{At} in X_1 and e^{-At} in X_2), due to the base flow, contributes to the evolution of the fluid impulse. It should be noted that for the linear case, when only $p_{x_{10}}$ is present, p_{x_1} would decrease due to the decrease in both X_2 and ω_2, whereas for the case when only $p_{x_{20}}$ is present, the increase would be due to an increase in both X_1 and ω_1. For the nonlinear cases with viscous effects (figure 8 and figure 9) these arguments are no longer valid mainly due to the self-induced motion, as was explained in detail in § 4.3, even though there are some qualitative similarities.

The growth of the fluid impulse is composed of the growth of the disturbance amplitude as well as its geometrical scale. As it is difficult to distinguish between their individual contributions: a direct comparison with other instability criteria is not straightforward. In the following we attempt to correlate the growth (and decay) of the fluid impulse with that of the disturbance kinetic energy (KE). The KE of a disturbance is commonly defined as $KE = \frac{1}{2}\int \boldsymbol{u}\cdot\boldsymbol{u}\,\mathrm{d}V$, also called the self-energy of the vortex structure (Leonard 2000). The KE for the highly nonlinear cases ($\varepsilon = 50$) presented in § 4.3 is evaluated from the numerical results and plotted along with the prediction of the linear inviscid theory in figure 12(a) and 12(b) corresponding to cases (a) and (b), respectively. Accordingly, the disturbance KE is calculated by converting (4.1) into Fourier space and numerically integrating it for the inviscid case. In this figure the calculated KE (presented as $\ln KE$) is shown by solid lines and the numerical results by symbols and both are normalized by their initial values. It can be seen that the numerical results have the same trends as the theoretical curves, i.e. decrease and increase monotonically for cases (a) and (b), respectively. In both cases the inviscid linear theory over-predicts the numerical results, indicating that viscosity and nonlinearity have a stabilizing effect. All results seem to follow an exponential decay in case (a) and growth in case (b). Comparing it with the growth of the fluid impulse, the KE for these nonlinear disturbances decreases when the fluid impulse decreases (figure 9a) and increases when the fluid impulse increases (figure 9b). The

correspondence between them, as well as with the enstrophy, suggests the use of the fluid impulse to predict the stability of a localized disturbance.

In this respect, the studies by Farrell (1989) and Criminale *et al.* (1994) should be mentioned. They assumed the initial disturbances to have an even-function distribution of vorticity (monopole) and therefore, unlike for the dipole structure considered in the present case, the initial fluid impulse was identically zero. This may explain why in those studies the flow was found to be neutrally stable when an energy criterion was used.

Finally, we would like to draw attention to the similarity between the growth of the CVP along the principal axis X_1 in the present case and the growth of 'rib' vortices observed in the braid region of a turbulent mixing layer (Bernal & Roshko 1986), in between two spanwise (Kelvin–Helmholtz) rollers in plane stagnation flow. In this case, the initial growth of the vortex pairs is along the direction connecting the bottom of the upstream roller and the top of the downstream one.

6. Conclusions

The components of the fluid impulse along the principal axes X_1 ($\mathrm{X}=\mathrm{Y}$) and X_2 ($\mathrm{X}=-\mathrm{Y}$), of a finite-amplitude localized disturbance in an irrotational plane stagnation flow, having an initial dipole Gaussian vorticity distribution, are respectively, predicted to decay and grow with time. The results are confirmed numerically for both linear and nonlinear disturbances.

The fluid impulse is found to be a suitable characteristic describing the temporal evolution of localized vortical disturbances. Furthermore, the correspondence between the growth/decay trends of the self-energy of the vortex structure (KE) and its associated fluid impulse suggests that the growth of the fluid impulse can be used as an instability criterion for such disturbances.

The solution of the linear viscous vorticity disturbance equation (Leonard 2000) predicts well the vorticity distribution for the linear case, but fails to predict the essential characteristics of a nonlinear disturbance associated with its self-induced movement. In both linear and nonlinear cases, the final structure is that of a counter-rotating vortex stretched along the principal axis $X=Y$, in accordance with the fluid impulse prediction.

This research has been supported by the Israeli Science Foundation under Grant no. 412/00.

REFERENCES

Andreotti, B., Douady, S. & Couder, Y. 2001 An experiment on two aspects of the interaction between strain and vorticity. *J. Fluid Mech.* **444**, 151–174.

Batchelor, G. K. 1967 *An introduction to Fluid Dynamics*. Cambridge University Press.

Brattkus, K. & Davis, S. H. 1991 The linear stability of plane stagnation-point flow against general disturbances. *Q. J. Mech. Appl. Maths* **44**, 135–146.

Craik, A. D. D. & Criminale, W. O. 1986 Evolution of wavelike disturbances in shear flows: a class of exact solutions of the Navier–Stokes equations. *Proc. R. Soc. Lond.* A **406**, 13–26.

Criminale, W. O., Jackson, T. L. & Lasseigne, D. G. 1994 Evolution of disturbances in stagnation-point flow. *J. Fluid Mech.* **270**, 331–347.

Farrell, B. F. 1989 Transient development in confluent and diffluent flow. *J. Atmos. Sci.* **46**, 3279–3288.

Kerr, O. S. & Dold, J. W. 1994 Periodic steady vortices in stagnation-point flow. *J. Fluid Mech.* **276**, 307–325.

Kevlahan, N. K. R. & Hunt, J. C. R. 1997 Nonlinear interations in turbulence with strong irrotational straining. *J. Fluid Mech.* **337**, 333–364.

Kida, S. 1981 Motion of an elliptic vortex in a uniform shear flow. *J. Phys. Soc. Japan* **50**, 3517–3520.

Lagnado, R. R., Phan-Thien, N. & Leal, L. G. 1984 The stability of two-dimensional linear flows. *Phys. Fluids* **27**, 1094–1101.

Leonard, A. 2000 *Turbulence Structure and Vortex Dynamics*. Cambridge University Press.

Levinski, V. & Cohen, J. 1995 The evolution of a localized vortex disturbance in extrenal shear flows. part 1. Theoretical considerations and preliminary experimental results. *J. Fluid Mech.* **289**, 159–177.

Lin, S. J. & Corcos, G. M. 1984 The mixing layer: deterministic models of a turbulent flow. Part 3. The effect of plane strain on the dynamics of streamwise vortices. *J. Fulid Mech.* **141**, 139–178.

Lyell, M. J. & Huerre, P. 1985 Linear and non linear stability of plane stagnation flow. *J. Fluid Mech.* **161**, 295–312.

Marshal, J. S. & Grant, J. R. 1994 Evolution and breakup of vortex rings in a straining and shearing flows. *J. Fluid Mech.* **273**, 285–312.

Neu, J. C. 1984 The dynamics of a columnar vortex in an imposed strain. *Phys. Fluids* **27**, 2397–2402.

Roberts, P. H. 1972 A hamiiltonian theory for weakly interacting vortices. *Mathematika* **19**, 169–179.

Saffman, P. G. 1992 *Vortex Dynamics*. Cambridge University Press.

Suponitsky, V., Cohen, J. & Bar-Yoseph, P. Z. 2005 The generation of streaks and hairpin vortices from a localized vortex embedded in unbounded uniform shear flow. *J. Fluid Mech.* **535**, 65–100.

Taylor, G. I. 1934 Evolution of disturbance in stagnation-point flow. *Proc. R. Soc.* **29**, 501–523.

Wilson, S. D. R. & Gladwell, I. 1978 The stability of a two-dimensional stagnation flow to three-dimensional disturbances. *J. Fluid Mech.* **84**, 517–527.